

## Bismuth substituted strontium cobalt perovskites for catalyzing oxygen evolution

Denis A. Kuznetsov,<sup>1,2,7</sup> Jiayu Peng,<sup>2,3,7</sup> Livia Giordano,<sup>1,2,4,6</sup> Yuriy Román-Leshkov,<sup>5</sup> and Yang Shao-Horn<sup>1,2,3,4,8,\*</sup>

<sup>1</sup>*Research Laboratory of Electronics,* <sup>2</sup>*Electrochemical Energy Laboratory,* <sup>3</sup>*Department of Materials Science and Engineering,* <sup>4</sup>*Department of Mechanical Engineering,* <sup>5</sup>*Department of Chemical Engineering, Massachusetts Institute of Technology, 77 Massachusetts Avenue, Cambridge, MA 02139, USA*

<sup>6</sup>*Dipartimento di Scienza dei Materiali, Università di Milano-Bicocca, Milano 20126, Italy*

<sup>7</sup>*These authors contributed equally*

<sup>8</sup>*Lead Contact*

*\*Correspondence: shaohorn@mit.edu*

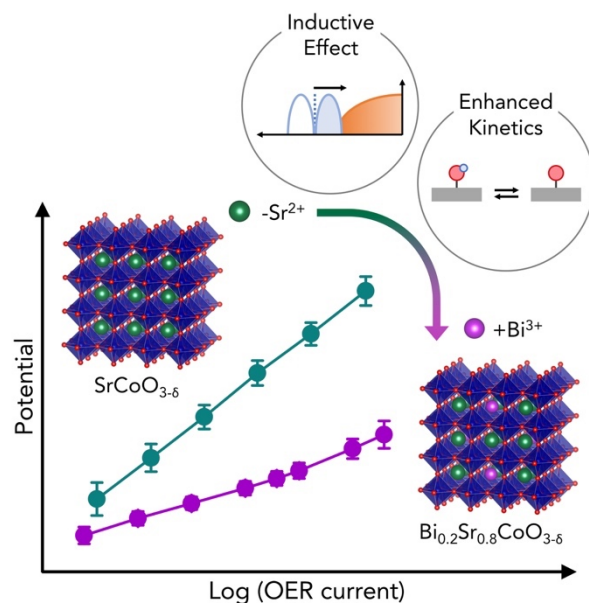
### SUMMARY

In this study, we employ the strategy of substitution with more electronegative/acidic A-site ions in the cobalt perovskites to alter O 2p-band center, surface hydroxide affinity, and oxygen evolution reaction (OER) activity and stability in the basic electrolyte. Galvanostatically charged  $\text{Bi}_{0.2}\text{Sr}_{0.8}\text{CoO}_{3-\delta}$  ( $\delta$  close to zero) was shown to exhibit record OER specific activity exceeding not only  $\text{La}_x\text{Sr}_{1-x}\text{CoO}_{3-\delta}$  but also charged  $\text{SrCoO}_{3-\delta}$  ( $\delta$  close to zero), one of the most active oxide OER catalysts reported so far. The enhanced OER activity of charged  $\text{Bi}_{0.2}\text{Sr}_{0.8}\text{CoO}_{3-\delta}$  can be attributed to greater hydroxide affinity facilitating the deprotonation of surface bound intermediates due to the presence of strong Lewis acidic A-site  $\text{Bi}^{3+}$  ions, while the high stability can result from lowered O 2p-band center relative to the Fermi level. This work provides a novel example in the rational design of highly active oxide catalysts for OER by leveraging the inductive effect.

## KEYWORDS

inductive effect; metal substitution; bismuth; transition metal oxides; perovskites; energy conversion; electrocatalysis; oxygen evolution reaction (OER)

## GRAPHICAL ABSTRACT



## INTRODUCTION

The distribution and on-demand use of electrical energy from sustainable resources, such as solar energy, requires storage technologies that are cost effective and involving earth-abundant elements. Solar energy can be stored in the form of chemical bonds by electrochemical water splitting to produce hydrogen,<sup>1,2</sup> or  $\text{CO}_2$  reduction to CO, methanol and hydrocarbons<sup>3,4</sup> as energy carriers, where oxygen evolution reaction (OER) is required to accompany above cathodic transformations. These technologies are advantageous to lithium ion batteries for large-scale storage as they have high gravimetric energy,<sup>5,6</sup> and chemical bonds used for energy storage involve elements (such as O, H, C) that are among the most abundant in the planet. In contrast, energy storage with current Li-ion batteries

requires storing each electron using one transition metal ion, and thus powering the planet with this technology is limited by the availability of metals such as cobalt and nickel in the earth crust.<sup>7</sup> The efficiency of the storage technologies based on  $H_2/CO/CH_3OH/C_nH_{2n+2}$  production is, however, severely limited to a significant extent by the sluggish reaction kinetics of OER,<sup>8–10</sup> which is catalyzed by precious metal catalysts such as  $RuO_2$ <sup>11,12</sup> and  $IrO_2$ .<sup>11,13,14</sup> The development of active OER electrocatalysts composed of earth-abundant elements<sup>15</sup> is therefore crucial for the large-scale implementation of these technologies.<sup>16</sup>

Late first-row transition metal oxides<sup>17–22</sup> based on cobalt,<sup>23,24</sup> nickel<sup>25–28</sup> and iron<sup>29,30</sup> are reported to be the most active to catalyze OER in basic solution. Experimental and computational studies in the past decade have been focusing on elucidating OER mechanisms<sup>8,9</sup> and identifying activity and stability descriptors,<sup>31–33</sup> which can be used to design better catalysts. Perovskites ( $ABO_{3-\delta}$ ) with immense structural, chemical and electronic flexibility associated with vast selections of A-site and B-site metal ions and oxygen deficiency<sup>34</sup> have been used to develop design principles of OER activity<sup>33,34</sup> and stability.<sup>35,36</sup> Recent work<sup>37</sup> has shown that lowering charge-transfer gap or increasing metal-oxygen covalency in perovskites can improve the OER kinetics, which is facilitated by first lowering the energetic barrier of electron transfer for the semiconducting oxides, reducing adsorption strength of oxygenated intermediates of OER<sup>38</sup> and then decreasing the energetic barriers<sup>34,37</sup> associated with OER steps on the surface of metallic oxides including the most active catalysts. Unfortunately, reducing the charge-transfer gap of these perovskites also lowers the Fermi level on the absolute energy scale, making it below the OER redox potential in the basic solution for the most active catalysts such as  $La_{0.5}Sr_{0.5}CoO_{3-\delta}$ .<sup>37</sup> This can generate more negatively charged surface and therefore result in weaker hydroxide affinity,<sup>17,39,40</sup> which can impede surface deprotonation during OER in basic solution (such as  $M-OH_{ad} + OH^- \rightarrow M-O_{ad} + H_2O + e^-$ ).<sup>37</sup> Therefore, tuning the

affinity towards hydroxide ions on these highly active oxide surfaces (e.g. by phosphate functionalization)<sup>41</sup> represents new opportunities to further enhance the OER performance.

In this work, we explored the substitution of A-site ions with high electronegativity or Lewis acidity in the cobalt perovskites to maintain high Co-O covalency by the inductive effect,<sup>28</sup> and potentially increase hydroxide affinity on the surface by introducing highly Lewis acidic ions to facilitate OER kinetics. This argument is supported by the enhanced OER kinetics previously observed for  $\text{LnNiO}_3$  perovskite series upon the substitution of  $\text{La}^{3+}$  with more electronegative  $\text{Gd}^{3+}$  and  $\text{Eu}^{3+}$ .<sup>42</sup> Herein we examine the OER activity of bismuth-substituted strontium cobalt perovskites,  $\text{Bi}_{0.2}\text{Sr}_{0.8}\text{CoO}_{3-\delta}$ , where the  $\text{Bi}^{3+}$  substituents possess the highest Lewis acidity (i.e. highest electronegativity) among 2+/3+ A-site ions,<sup>43</sup> with a  $\text{pK}_a$  value of 1.58 much lower than that of other commonly used A-site metals in cobalt-based perovskite oxides (e.g.  $\text{pK}_a([\text{Sr}^{2+}(\text{H}_2\text{O})_n]) = 13.18$ ,  $\text{pK}_a([\text{La}^{3+}(\text{H}_2\text{O})_n]) = 9.06$ ,  $\text{pK}_a([\text{Pr}^{3+}(\text{H}_2\text{O})_n]) = 8.55$ ). Remarkably,  $\text{Bi}_{0.2}\text{Sr}_{0.8}\text{CoO}_{3-\delta}$  that was galvanostatically charged to minimize oxygen vacancies was shown to exhibit an exceptionally low Tafel slope ( $\sim 25 \text{ mV decade}^{-1}$ ) and higher intrinsic OER activity than  $\text{La}_{1-x}\text{Sr}_x\text{CoO}_{3-\delta}$  and charged  $\text{SrCoO}_{3-\delta}$  (one of the most active catalysts reported to date)<sup>38,44</sup> at high current densities ( $> \sim 1 \text{ mA cm}^{-2}_{\text{oxide}}$ ). The record intrinsic OER activity can be rationalized by stronger affinity towards hydroxide during surface deprotonation associated with more acidic  $\text{Bi}^{3+}$  than  $\text{La}^{3+}$  and  $\text{Sr}^{2+}$ , and comparable Co-O covalency to  $\text{SrCoO}_{3-\delta}$  as shown from density functional theory (DFT) calculations. In addition, no amorphization or changes in the composition were observed for the surface of charged  $\text{Bi}_{0.2}\text{Sr}_{0.8}\text{CoO}_{3-\delta}$  after OER, with such high structural stability being attributed to the lowered O 2p-band center relative to the Fermi level of  $\text{Bi}_{0.2}\text{Sr}_{0.8}\text{CoO}_{3-\delta}$  than that of  $\text{SrCoO}_{3-\delta}$ . Tuning of the electronic structure and surface acid-base chemistry through inductive effect associated with rational metal substitution represents a new strategy for enhancing the activity and stability of OER catalysts.

## RESULTS AND DISCUSSION

Pristine  $\text{Bi}_{0.2}\text{Sr}_{0.8}\text{CoO}_{3-\delta}$  was synthesized through a conventional solid-state route starting from  $\text{Bi}_2\text{O}_3$ ,  $\text{CoO}$  and  $\text{SrCO}_3$  precursors<sup>45</sup> as detailed in Supplemental Experimental Procedure. Higher levels of bismuth substitution were not explored due to previously reported solubility limit of  $\sim 20\%$ <sup>45</sup> and the need to have high Co oxidation state (close to  $4+$ ) to achieve high OER activities.<sup>46</sup> Refinement of the powder X-ray diffraction (PXRD) pattern (Figure 1) confirmed a cubic structure with Pm-3m space group and a unit cell parameter of  $3.896 \text{ \AA}$  (Table S1), which is comparable to that reported in the original study ( $\sim 3.9 \text{ \AA}$ ).<sup>45</sup> As previous neutron diffraction refinements and cobalt oxidation state ( $\sim 3$ ) based on iodometric titrations<sup>45</sup> revealed the oxygen vacancy content,  $\delta \approx 0.4$ , for pristine  $\text{Bi}_{0.2}\text{Sr}_{0.8}\text{CoO}_{3-\delta}$ , we estimated  $\delta \approx 0.4$  for the oxygen deficiency for our as-synthesized pristine  $\text{Bi}_{0.2}\text{Sr}_{0.8}\text{CoO}_{3-\delta}$  sample. This argument is further supported by the Co K-edge X-ray absorption spectroscopy (XAS). The cobalt oxidation state of  $\sim 2.96$  for pristine  $\text{Bi}_{0.2}\text{Sr}_{0.8}\text{CoO}_{3-\delta}$  determined from the position of Co K-edge (Figure S1) is in qualitative agreement with the estimated oxygen vacancy level ( $\delta \approx 0.4$ ).

We further reduced the oxygen deficiency in  $\text{Bi}_{0.2}\text{Sr}_{0.8}\text{CoO}_{3-\delta}$  by galvanostatic charging in  $\text{O}_2$ -saturated  $1 \text{ M KOH}$  (Figure S2), as having high covalency for Co-O bonds associated with the presence of  $\text{Co}^{4+}$  is needed to obtain high intrinsic OER activity.<sup>37,38</sup> Electrochemical oxygen intercalation into the perovskite structure can take place during galvanostatic charging to fill the oxygen vacancies in oxygen-deficient perovskites,<sup>47,48</sup> such as  $\text{SrCoO}_{3-\delta}$ ,<sup>38,49</sup> upon slow oxidation in basic solutions. During charging, two voltage plateaus were observed for thin-film  $\text{Bi}_{0.2}\text{Sr}_{0.8}\text{CoO}_{3-\delta}$  deposited on glassy carbon (GC) electrodes, similar to those reported for  $\text{La}_{0.5}\text{Sr}_{0.5}\text{CoO}_{3-\delta}$ <sup>38</sup> and  $\text{SrCoO}_{3-\delta}$ <sup>38,47</sup> (plateaus more defined in the latter case, Figure S3), which can be attributed to the filling of oxygen vacancies ( $\text{Bi}_{0.2}\text{Sr}_{0.8}\text{CoO}_{3-\delta} + 2\delta\text{OH}^- \rightarrow \text{Bi}_{0.2}\text{Sr}_{0.8}\text{CoO}_3 + \delta\text{H}_2\text{O} + 2\delta\text{e}^-$ ). These redox events

were reflected by the two redox peaks centered at ~1.1 and ~1.3 V vs. reversible hydrogen electrode (RHE) in the cyclic voltammetry (CV) measurements (Figure 2). Similar redox features have been reported for other Co-based catalysts such as CoOOH (in 1 M KOH),<sup>23</sup> and LiCoO<sub>2</sub> (in 0.1 M KOH),<sup>50,51</sup> which have been attributed to Co<sup>2+</sup>/Co<sup>3+</sup> and Co<sup>3+</sup>/Co<sup>4+</sup> redox couples, respectively. The oxygen intercalation into the bulk structure of Bi<sub>0.2</sub>Sr<sub>0.8</sub>CoO<sub>3-δ</sub> upon charging is supported by the reduction in the lattice parameter of the perovskite structure for Bi<sub>0.2</sub>Sr<sub>0.8</sub>CoO<sub>3-δ</sub> pellet electrodes (without carbon and binder) after galvanostatic charging as revealed by PXRD analysis (Figure 1), indicative of increased Co oxidation state associated with oxygen deficiency reduction. Charged Bi<sub>0.2</sub>Sr<sub>0.8</sub>CoO<sub>3-δ</sub> (with one electron passed per formula unit at a C-rate of C/50 or C/20, Figure S2) was found to have smaller unit cell parameters  $a = 3.835 \text{ \AA}$  (C/50 charging) and  $a = 3.838 \text{ \AA}$  (C/20 charging) than that of pristine Bi<sub>0.2</sub>Sr<sub>0.8</sub>CoO<sub>3-δ</sub> ( $a = 3.896 \text{ \AA}$ ). Although the exact value of oxygen deficiency  $\delta$  on the surface of charged Bi<sub>0.2</sub>Sr<sub>0.8</sub>CoO<sub>3-δ</sub> during OER is not known, it is proposed that  $\delta$  value is close to zero, especially for the C/50 sample. This hypothesis is supported by the following observations. First, ~0.8 e<sup>-</sup> per formula unit passed before the OER plateau at 1.4 V vs. RHE<sup>38</sup> (Figure S3), which would result in a fully stoichiometric perovskite structure based on the oxygen deficiency level in pristine Bi<sub>0.2</sub>Sr<sub>0.8</sub>CoO<sub>3-δ</sub> ( $\delta \approx 0.4$ ). Second, the slower galvanostatic charging typically imparts smaller oxygen deficiency in Bi<sub>0.2</sub>Sr<sub>0.8</sub>CoO<sub>3-δ</sub> and other perovskites.<sup>38</sup> As the oxygen intercalation kinetics and oxygen ion transport in perovskites are slow, the surfaces of charged Bi<sub>0.2</sub>Sr<sub>0.8</sub>CoO<sub>3-δ</sub> can have even smaller  $\delta$  than the bulk for given charging rates. Third, C/50 galvanostatically charged Bi<sub>0.2</sub>Sr<sub>0.8</sub>CoO<sub>3-δ</sub> was found to have much greater OER activity than pristine Bi<sub>0.2</sub>Sr<sub>0.8</sub>CoO<sub>3-δ</sub> (Figure S3). This enhanced OER kinetics can be attributed to greater Co oxidation state on the surface, which is expected from the previously reported correlations<sup>32,37,38,44,49</sup> demonstrating that lowering the cobalt 3d band with respect to the oxygen 2p-band center (i.e. lowering the charge-transfer gap) by

increasing the nominal oxidation state of cobalt is correlated with increasing specific OER activity of cobalt-based perovskites. Therefore, we will focus on the OER kinetics of C/50 charged  $\text{Bi}_{0.2}\text{Sr}_{0.8}\text{CoO}_{3-\delta}$  further in this work.

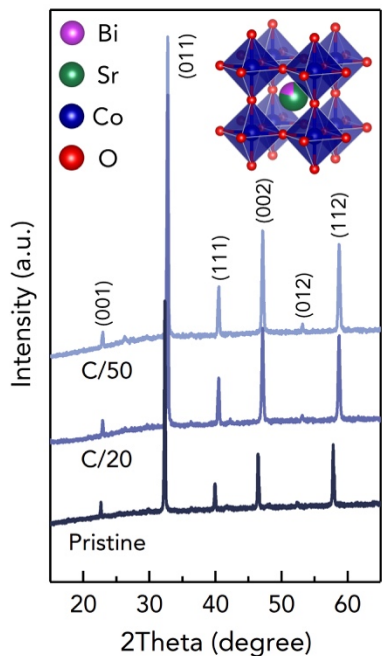


**Figure 1. Powder X-ray Diffraction (PXRD) Spectra**

PXRD patterns of pristine oxygen-deficient  $\text{Bi}_{0.2}\text{Sr}_{0.8}\text{CoO}_{3-\delta}$  powder, as well as  $\text{Bi}_{0.2}\text{Sr}_{0.8}\text{CoO}_{3-\delta}$  galvanostatically charged at  $6.1 \text{ mA g}^{-1}$  for 20 hr (C/20), and at  $2.4 \text{ mA g}^{-1}$  for 50 hr (C/50). Patterns were indexed in a cubic unit cell with space group Pm-3m. All spectra were collected for powder samples ( $\sim 0.3 \text{ g}$ ), in a continuous scan mode with a scan rate of 2 degrees per min, and a scan range from  $15^\circ$  to  $65^\circ$ . Lattice parameters as assessed by PXRD are consistent with those reported previously.<sup>45</sup> The samples were quenched to room temperature after every heat treatment during the solid-state synthesis to minimize the presence of the minor secondary phase of  $\text{Bi}_2\text{Sr}_2\text{Co}_3\text{O}_y$ ,<sup>45,52</sup> which could be detected by peaks between  $24^\circ$  and  $30^\circ$  on the PXRD spectra (with estimated volume fraction of less than 1.7%). Galvanostatic charging experiments were performed for pelletized  $\text{Bi}_{0.2}\text{Sr}_{0.8}\text{CoO}_{3-\delta}$  powder (60 mg, 5 mm diameter pellet) attached to a graphene sheet (0.120 mm thickness) in  $\text{O}_2$ -saturated 1 M KOH electrolyte. Inset shows the schematic representation of the crystal structure of  $\text{Bi}_{0.2}\text{Sr}_{0.8}\text{CoO}_{3-\delta}$ .

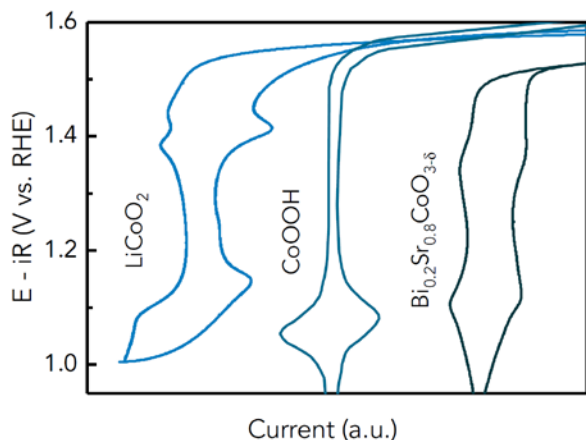


**Figure 2. Electrochemical Redox Behavior of Co-Based Oxides**

CV curve of C/50 charged thin-film  $\text{Bi}_{0.2}\text{Sr}_{0.8}\text{CoO}_{3-\delta}$  supported on glassy carbon electrode ( $0.25 \text{ mg}_{\text{oxide}} \text{ cm}^{-2}_{\text{disk}}$ ) compared with previously reported CV curves of  $\text{LiCoO}_2$ <sup>28</sup> (0.1 M) and  $\text{CoOOH}$ <sup>23</sup> (1 M) in  $\text{O}_2$ -saturated KOH solutions (scan rate:  $10 \text{ mV s}^{-1}$ ).

The OER kinetics of charged  $\text{Bi}_{0.2}\text{Sr}_{0.8}\text{CoO}_{3-\delta}$  (thin films on GC, C/50 charging in  $\text{O}_2$ -saturated 1 M KOH, Figure S3) were assessed in  $\text{O}_2$ -saturated KOH solutions at different pHs through steady-state galvanostatic measurements (i.e. chronopotentiometry) instead of CV, as the contributions of current from electrochemical oxygen intercalation in bulk cannot be excluded from OER kinetic currents when using the CV measurements.<sup>38</sup> The specific activity was obtained by normalizing  $iR$ -corrected kinetic currents to the Brunauer-Emmett-Teller (BET) specific oxide surface area. The specific OER activity of charged  $\text{Bi}_{0.2}\text{Sr}_{0.8}\text{CoO}_{3-\delta}$  is much higher than those of  $\text{LaCoO}_3$ , charged  $\text{La}_{0.5}\text{Sr}_{0.5}\text{CoO}_{3-\delta}$  and  $\text{Pr}_{0.5}\text{Ba}_{0.5}\text{CoO}_{3-\delta}$ <sup>38</sup> in both 0.1 M and 1 M KOH (Figures 3A and S4), which can be attributed to greater Co-O covalency associated with higher Co oxidation state<sup>32,34,37,38,44</sup> expected for charged  $\text{Bi}_{0.2}\text{Sr}_{0.8}\text{CoO}_{3-\delta}$  ( $\delta$  close to zero for all these charged perovskites). Remarkably, the specific OER activity of charged  $\text{Bi}_{0.2}\text{Sr}_{0.8}\text{CoO}_{3-\delta}$  was found to be comparable to charged  $\text{SrCoO}_{3-\delta}$  at low current densities, and much greater at high current densities due to an exceptionally low Tafel slope of  $\sim 25 \text{ mV decade}^{-1}$  as compared to other oxide catalysts<sup>20,25,33</sup> (e.g.  $\sim 60 \text{ mV decade}^{-1}$  for charged  $\text{SrCoO}_{3-\delta}$ ).<sup>38</sup> Moreover, charged



$\text{Bi}_{0.2}\text{Sr}_{0.8}\text{CoO}_{3-\delta}$  exhibited pH-dependent OER activity on the RHE scale, where the specific activity increased with increasing pH (Figures 3B and S6). Similar pH-dependent OER kinetics have been reported for charged  $\text{La}_{0.5}\text{Sr}_{0.5}\text{CoO}_{3-\delta}$ ,  $\text{Pr}_{0.5}\text{Ba}_{0.5}\text{CoO}_{3-\delta}$  and  $\text{SrCoO}_{3-\delta}$ ,<sup>38</sup> which cannot be explained by the conventional OER mechanism<sup>8,9,53,54</sup> with four concerted proton-coupled electron transfer (PCET) steps. Instead, OER kinetics on these highly active and covalent oxides are limited by proton transfer, which is decoupled from electron transfer.<sup>37</sup> In contrast, less active  $\text{LaCoO}_3$ <sup>38</sup> exhibits pH-independent OER activity on the RHE scale expected from the conventional concerted PCET pathways.<sup>37</sup> Notably, charged  $\text{Bi}_{0.2}\text{Sr}_{0.8}\text{CoO}_{3-\delta}$  exhibits OER currents one order of magnitude higher than those of fully charged  $\text{SrCoO}_{3-\delta}$  at 1.55 V vs. RHE for all pHs examined (Figure 3B). Possible physical origins for the record high OER activity are discussed below together with processes responsible for its pH-dependent OER activity on the RHE scale.

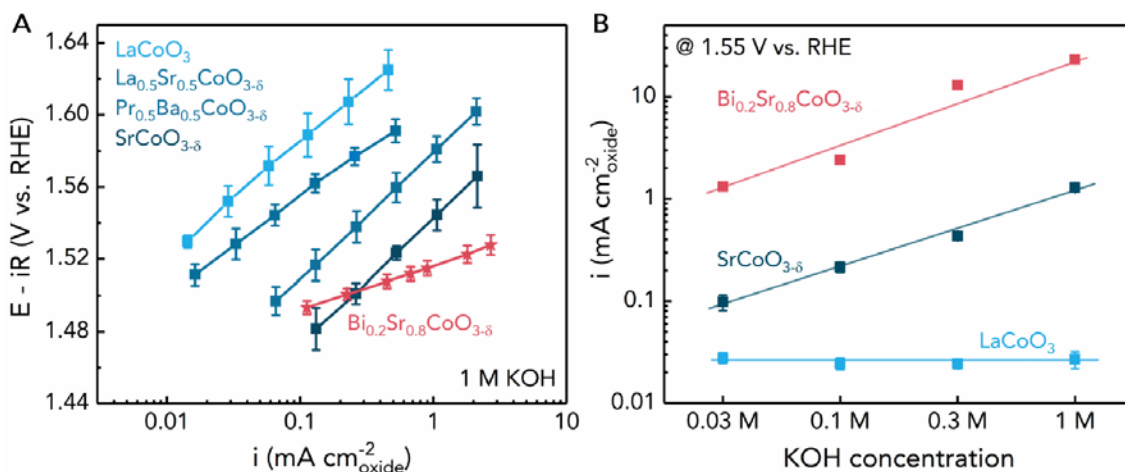


**Figure 3. Record and pH-Dependent Intrinsic OER Activity of Fully Charged  $\text{Bi}_{0.2}\text{Sr}_{0.8}\text{CoO}_{3-\delta}$**

(A) Tafel plots for selected Co-based perovskite oxides. Measurements were performed in  $\text{O}_2$ -saturated 1 M KOH electrolyte with an oxide loading of  $0.25 \text{ mg}_{\text{oxide}} \text{ cm}^{-2}_{\text{disk}}$ . Data points were all extracted from steady-state galvanostatic OER measurements. Data for  $\text{LaCoO}_3$ , galvanostatically charged  $\text{La}_{0.5}\text{Sr}_{0.5}\text{CoO}_{3-\delta}$ ,  $\text{Pr}_{0.5}\text{Ba}_{0.5}\text{CoO}_{3-\delta}$  and  $\text{SrCoO}_{3-\delta}$  (having  $\delta$  close to zero) were taken from our previous work.<sup>38</sup>

(B) Specific OER activity at 1.55 V vs. RHE as a function of KOH concentration measured for glassy carbon electrodes with an oxide loading of  $0.25 \text{ mg}_{\text{oxide}} \text{ cm}^{-2}_{\text{disk}}$ . Data for fully charged  $\text{Bi}_{0.2}\text{Sr}_{0.8}\text{CoO}_{3-\delta}$  were extracted from the OER Tafel plot shown in Figure S6. Data points for 0.3 M and 1 M KOH were obtained by the extrapolation of linear Tafel regions to higher potentials.

The high OER activity of charged  $\text{Bi}_{0.2}\text{Sr}_{0.8}\text{CoO}_{3-\delta}$  exceeding that of charged  $\text{SrCoO}_{3-\delta}$  can be attributed in part to having comparable Co-O covalency to  $\text{SrCoO}_{3-\delta}$  due to the inductive effect<sup>28</sup> introduced by substituting  $\text{Sr}^{2+}$  with strongly Lewis acidic  $\text{Bi}^{3+}$  ( $\text{pK}_a$  for  $[\text{Bi}(\text{H}_2\text{O})_n]^{3+}$  ions is 1.58).<sup>43</sup> Despite the fact that having lower nominal Co oxidation state in charged  $\text{Bi}_{0.2}\text{Sr}_{0.8}\text{CoO}_{3-\delta}$  (3.8+) than charged  $\text{SrCoO}_{3-\delta}$  (4+) is expected to impart lower OER activity than  $\text{SrCoO}_{3-\delta}$  based on previous reported correlation,<sup>32,37,38,44</sup>  $\text{Bi}^{3+}$  ions with much higher electronegativity can pull more electron density from cobalt than other divalent/trivalent A-site ions with lower electronegativity (e.g.,  $\text{Sr}^{2+}$ ,  $\text{La}^{3+}$ ), lowering the energy of cobalt 3d band (i.e. antibonding orbitals of cobalt-ligand bonds)<sup>28</sup> and thus leading to retained high Co-O covalency upon bismuth substitution (Figures 4A and 4B). This argument is supported by our computed density of states for fully stoichiometric  $\text{Bi}_{0.125}\text{Sr}_{0.875}\text{CoO}_3$  and  $\text{Bi}_{0.25}\text{Sr}_{0.75}\text{CoO}_3$  (Figure S9), where the energy difference between the Co 3d-band center and the O 2p-band center, a measure of the covalency for the cobalt-oxygen bonds,<sup>37,38</sup> remains unchanged relative to stoichiometric  $\text{SrCoO}_3$  (Figure 4B). Having high metal-ligand covalency for perovskite oxides is key to promote OER kinetics by enabling the surface deprotonation of reaction intermediates by hydroxide ions decoupled from electron transfer which limits the OER kinetics.<sup>37</sup> Moreover, the lattice oxygen sites of oxides on the surface can be possibly activated and participate in OER in addition to surface metal ions.<sup>38</sup>

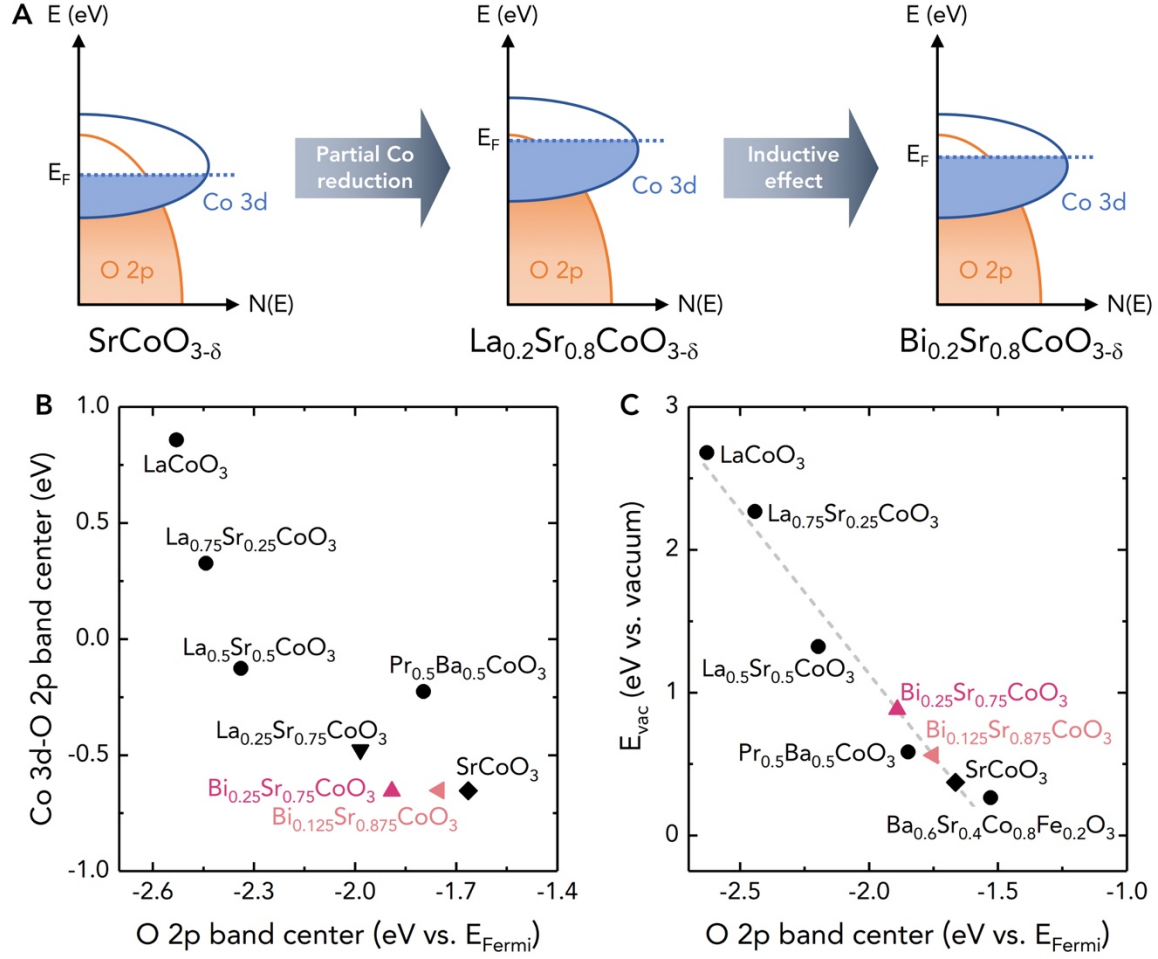


**Figure 4. Bulk Electronic Structures of Fully Charged  $\text{Bi}_{0.2}\text{Sr}_{0.8}\text{CoO}_{3-\delta}$**

(A) Schematic illustration of the changes in electronic structures upon bismuth substitution from charged  $\text{SrCoO}_{3-\delta}$  to charged  $\text{Bi}_{0.2}\text{Sr}_{0.8}\text{CoO}_{3-\delta}$  (both having  $\delta \approx 0$ ).

(B) Difference between the Co 3d-band center and the O-2p band center versus the O-2p band center relative to the Fermi level for different stoichiometric cobalt-based perovskites computed at DFT + U level. Both oxygen 2p-band and cobalt 3d-band centers were determined by taking the centroid of the projected density of states of O 2p and cobalt 3d states (both occupied and unoccupied states) relative to the Fermi level. The calculation results of  $\text{LaCoO}_3$ ,  $\text{La}_{0.5}\text{Sr}_{0.5}\text{CoO}_3$ ,  $\text{Pr}_{0.5}\text{Ba}_{0.5}\text{CoO}_3$  have been reported in our previous work.<sup>38</sup> The calculation results of  $\text{La}_{0.75}\text{Sr}_{0.25}\text{CoO}_3$  have been reported in our previous work.<sup>72</sup>

(C) Computed oxygen vacancy formation energy ( $E_{\text{vac}}$  vs. vacuum, relative to  $\text{O}_2$ ) compared to the computed oxygen 2p-band center relative to the Fermi level for  $\text{LaCoO}_3$ ,  $\text{La}_{0.75}\text{Sr}_{0.25}\text{CoO}_3$ ,  $\text{La}_{0.5}\text{Sr}_{0.5}\text{CoO}_3$ ,  $\text{Pr}_{0.5}\text{Ba}_{0.5}\text{CoO}_3$ ,  $\text{SrCoO}_3$ , and  $\text{Ba}_{0.6}\text{Sr}_{0.4}\text{Co}_{0.2}\text{Fe}_{0.8}\text{O}_3$  with full oxygen stoichiometry, showing the nearly linear correlation between oxygen vacancy formation energetics and the oxygen 2p-band center relative to the Fermi level. This trend can be rationalized by the energetics associated with the creation of oxygen vacancies in the perovskite structure (Figure S15). The calculation results of  $\text{LaCoO}_3$ ,  $\text{La}_{0.5}\text{Sr}_{0.5}\text{CoO}_3$ ,  $\text{Pr}_{0.5}\text{Ba}_{0.5}\text{CoO}_3$ ,  $\text{SrCoO}_3$  ( $E_{\text{vac}}$  only), and  $\text{Ba}_{0.6}\text{Sr}_{0.4}\text{Co}_{0.2}\text{Fe}_{0.8}\text{O}_3$  have been reported in our previous work.<sup>38</sup> The calculation

results of  $\text{La}_{0.75}\text{Sr}_{0.25}\text{CoO}_3$  have been reported in our previous work.<sup>72</sup> The oxygen vacancy formation energy for fully stoichiometric  $\text{Bi}_{0.125}\text{Sr}_{0.875}\text{CoO}_3$  and  $\text{Bi}_{0.25}\text{Sr}_{0.75}\text{CoO}_3$  was further projected following the linear correlation and with the computed oxygen 2p-band centers of these two compounds.

Employing  $\text{Bi}^{3+}$  with high electronegativity or Lewis acidity can increase hydroxide affinity on the oxide surface, which can facilitate OER kinetics as the reaction kinetics on highly covalent oxides are limited by processes associated with the deprotonation of surface reaction intermediates.<sup>37</sup> Like other perovskites with high Co-O covalency,<sup>37</sup> charged  $\text{Bi}_{0.2}\text{Sr}_{0.8}\text{CoO}_{3-\delta}$  has the oxide Fermi level much lower than the thermodynamic OER redox potential energy in the basic solution (Figures 5A and 5B), which results in negatively charged oxide surfaces when equilibrated with the electrolyte. This negative charge on the surface of oxides can come from surface adsorption of hydroxide ions from the solution and/or redistribution of the electron density from the bulk to the surface. Specifically, high Co-O covalency and lowered charge-transfer gap increase bulk electron mobility leading to accumulation of the negative charges on the interface with electrolyte solution, making this mechanism favored over hydroxide adsorption,<sup>37,39,40</sup> thus imparting weaker hydroxide affinity to the oxide surface under equilibrium conditions. The presence of strongly electronegative  $\text{Bi}^{3+}$  at the oxide surface of charged  $\text{Bi}_{0.2}\text{Sr}_{0.8}\text{CoO}_{3-\delta}$  can enhance affinity towards hydroxide ions as compared to  $\text{SrCoO}_{3-\delta}$ , increase ionicity of the O-H bonds, and therefore facilitate chemical/electrochemical surface deprotonation during OER in basic solution (such as  $\text{M-OH}_{\text{ad}} + \text{OH}^- \rightarrow \text{M-O}_{\text{ad}} + \text{H}_2\text{O} + \text{e}^-$ ).<sup>37</sup> This argument is in agreement with the observed pH-dependent OER activity of charged  $\text{Bi}_{0.2}\text{Sr}_{0.8}\text{CoO}_{3-\delta}$  on the RHE scale (Figures 3B and S6), which can be rationalized by pathways involving acid-base equilibrium before the rate-limiting step,<sup>55</sup> and/or rate-limiting proton transfer decoupled from electron transfer.<sup>37,38,56</sup> Similar pH-dependent OER activity has been reported for Ni-Fe oxyhydroxides, which has been attributed to the non-concerted metal oxidation coupled with surface hydroxides deprotonation leading to formation of

negatively charged intermediates.<sup>57</sup> Here we argue that increasing pH (i.e. increasing hydroxide ion concentration in the solution) would promote the deprotonation of surface species like  $\text{M-OH}_{\text{ad}}$  by  $\text{OH}^-$  via mechanisms including either acid-base equilibrium before the rate-limiting step<sup>55</sup> or proton transfer decoupled from electron transfer as the rate-limiting step,<sup>37</sup> and/or electrochemical surface deprotonation with non-integer electron transfer,<sup>58–60</sup> which would lead to increased OER activity on the RHE scale with increasing pH. Further support came from the A-site-independent OER kinetics for those less covalent  $\text{LnCoO}_3$  perovskites ( $\text{Ln} = \text{La}, \text{Nd}, \text{Gd}, \text{Sm}, \text{Eu}$ ), where the OER kinetics are limited by electron transfer,<sup>37</sup> and having more Lewis acidic A-site ions did not induce any changes in the OER activity beyond experimental uncertainty (Figure S4).

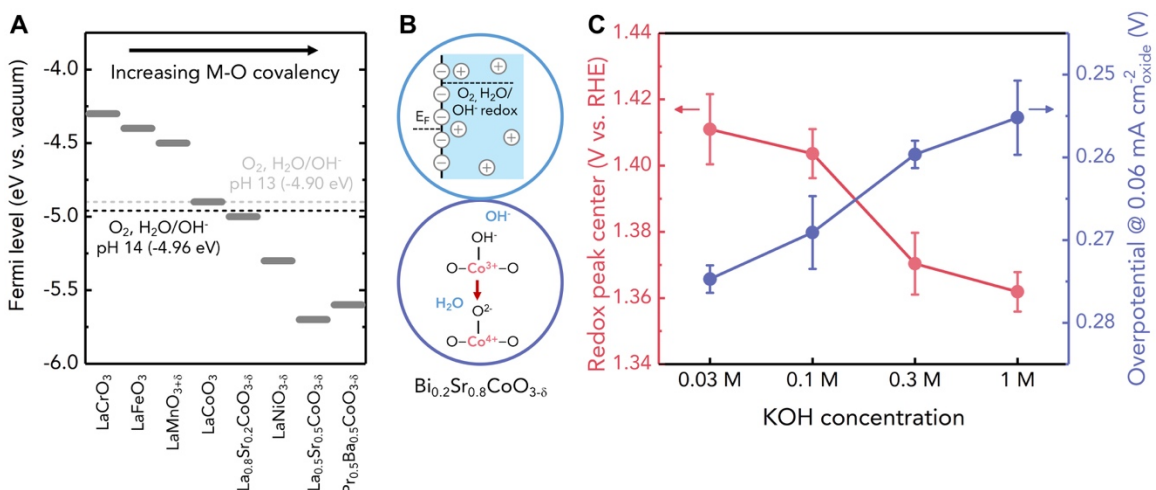


**Figure 5. pH-Dependent Pre-OER Cobalt Redox of Fully Charged  $\text{Bi}_{0.2}\text{Sr}_{0.8}\text{CoO}_{3-\delta}$**

(A) Trends in the Fermi level positions of perovskite oxides and corresponding hydroxide affinity at the oxide-electrolyte interface, which were estimated from X-ray spectroscopic data under rigid band assumption and have been reported in our previous work.<sup>37</sup> The hydroxide affinity is defined as the position of Fermi level relative to the  $\text{O}_2, \text{H}_2\text{O}/\text{OH}^-$  redox potential energy. With high metal-oxygen covalency, the oxide Fermi level lies below the OER potential energy, leading to negatively charged oxide surface when equilibrated with the electrolyte.

(B) Schematic illustration of the oxide-electrolyte interface and the electrochemical process that corresponds to the pre-OER  $\text{Co}^{3+}/\text{Co}^{4+}$  redox of fully charged  $\text{Bi}_{0.2}\text{Sr}_{0.8}\text{CoO}_{3-\delta}$ .

(C) Position of the average redox peak center prior to OER (left, red) and the OER overpotential (right, blue) estimated as the potential required to achieve  $\sim 0.06 \text{ mA cm}^{-2}_{\text{oxide}}$  OER current as assessed from galvanostatic

OER measurements for fully charged  $\text{Bi}_{0.2}\text{Sr}_{0.8}\text{CoO}_{3-\delta}$ , as a function of the KOH electrolyte concentration. CV measurements at different KOH concentrations were performed for  $\text{Bi}_{0.2}\text{Sr}_{0.8}\text{CoO}_{3-\delta}$  galvanostatically charged for 50 h in  $\text{O}_2$ -saturated 1 M KOH electrolyte with an oxide loading of  $0.25 \text{ mg}_{\text{oxide}} \text{ cm}^{-2}_{\text{disk}}$ .

The proposed explanation for the unprecedentedly high and pH-dependent OER activity of charged  $\text{Bi}_{0.2}\text{Sr}_{0.8}\text{CoO}_{3-\delta}$  is in agreement with its pH-dependent redox peak features at  $\sim 1.3 \text{ V}$  vs. RHE immediately prior to OER (Figures 5C, S10 and S11), which might suggest pH-dependent binding of OER reaction intermediates on the RHE scale. The redox peaks at  $\sim 1.3 \text{ V}$  vs. RHE can be assigned to the  $\text{Co}^{3+}/\text{Co}^{4+}$  redox reaction associated with electrochemical deprotonation of surface reaction intermediates such as  $\text{M-OH}_{\text{ad}}$  by  $\text{OH}^-$  in the solution to form  $\text{M-O}_{\text{ad}}$  species.<sup>61,62</sup> Similar shifts for pre-OER redox peaks have been found for Ni-Fe oxyhydroxides (up to  $-60 \text{ mV pH}^{-1}$ ),<sup>57</sup>  $\text{RuO}_2$  (101), (001), (001) surfaces (up to  $-27 \text{ mV pH}^{-1}$ )<sup>63</sup> and  $\text{IrO}_2$  (110) surface ( $\sim -7.5 \text{ mV pH}^{-1}$ ),<sup>64</sup> which have been attributed to the oxide-water interface structure changes at different pHs<sup>65</sup> or non-integer number of electrons transferred during this step.<sup>58–60</sup> Here we relate this pH-dependent redox peak shift to the energetics of hydroxide affinity established recently.<sup>37</sup> With decreasing pH, the electron energy associated with OER redox decreases on the absolute energy scale and moves closer to the oxide Fermi level (Figure 5A),<sup>37</sup> which reduces the accumulation of negative charges on the oxide surface and results in stronger hydroxide affinity and more effective surface deprotonation associated with  $\text{Co}^{3+}/\text{Co}^{4+}$  redox (Figure 5B), in agreement with the negative redox peak shift with increasing pH ( $\sim -40 \text{ mV pH}^{-1}$ ). Lastly, the Tafel slope ( $\sim 25 \text{ mV decade}^{-1}$ ) for charged  $\text{Bi}_{0.2}\text{Sr}_{0.8}\text{CoO}_{3-\delta}$  is considerably lower than the Tafel slopes of other highly covalent Co-based perovskites such as charged  $\text{La}_{0.5}\text{Sr}_{0.5}\text{CoO}_{3-\delta}$ ,  $\text{Pr}_{0.5}\text{Ba}_{0.5}\text{CoO}_{3-\delta}$  and  $\text{SrCoO}_{3-\delta}$  ( $\sim 60 \text{ mV decade}^{-1}$ ),<sup>38</sup> but comparable to those of perovskites that are known to amorphize upon leaching out A-site ions during OER ( $\sim 40 \text{ mV decade}^{-1}$ )<sup>66</sup> and Ni-Fe oxyhydroxides ( $\sim 30 \text{ mV decade}^{-1}$ ).<sup>67</sup> Such a low Tafel slope has been attributed previously<sup>68</sup> to having a chemical deprotonation as the rate-

limiting step for catalysts with high surface coverage of surface hydroxide ( $\text{M-OH}_{\text{ad}}$ ). Further in situ electrochemical diffraction<sup>69</sup> and spectroscopic<sup>70,71</sup> studies are needed to provide detailed insights into the surface species and reaction mechanisms as a function of potential.

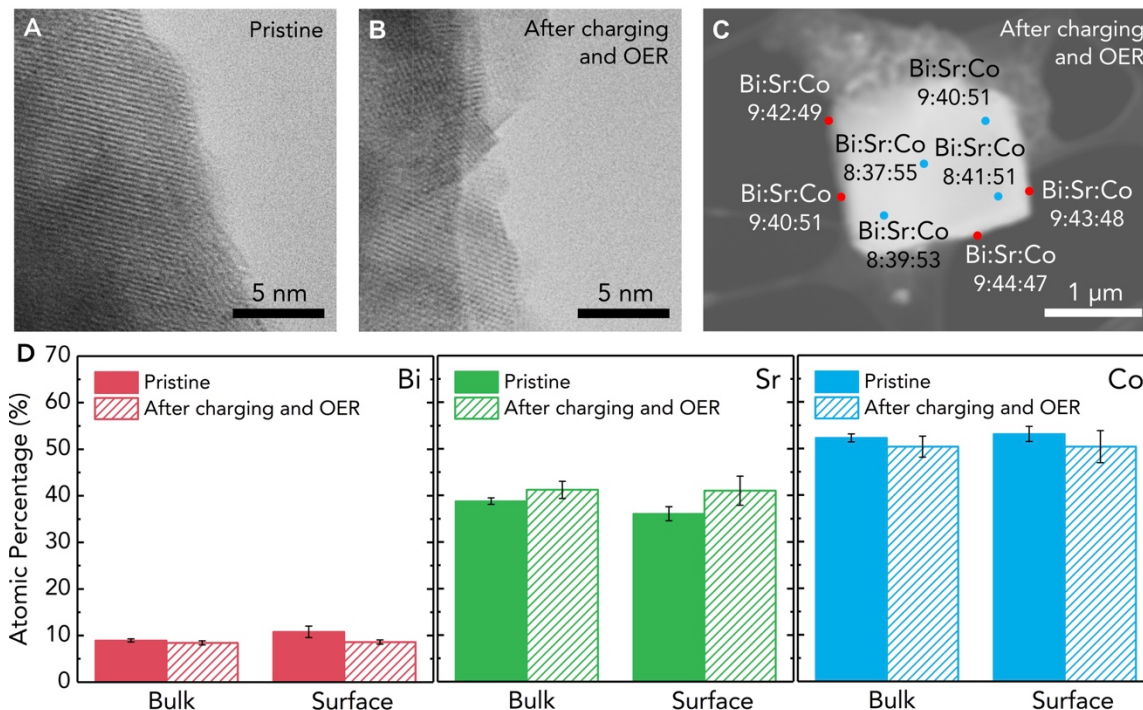


**Figure 6. High Surface Stability of  $\text{Bi}_{0.2}\text{Sr}_{0.8}\text{CoO}_{3-\delta}$  After Galvanostatic Charging and OER**

(A and B) HRTEM images of (A) pristine oxygen-deficient  $\text{Bi}_{0.2}\text{Sr}_{0.8}\text{CoO}_{3-\delta}$  powder, and (B) charged  $\text{Bi}_{0.2}\text{Sr}_{0.8}\text{CoO}_{3-\delta}$  followed by OER measurements. Galvanostatic charging were performed for oxides films containing Nafion and acetylene black carbon supported on a glassy carbon electrode at  $2.4 \text{ mA g}^{-1}$  for 50 hr in  $\text{O}_2$ -saturated 1 M KOH electrolyte with an oxide loading of  $0.25 \text{ mg}_{\text{oxide}} \text{ cm}^{-2}_{\text{disk}}$ .

(C) Representative high-angular annular dark-field scanning transmission electron microscopy (HAADF-STEM) imaging and corresponding EDX analysis of fully charged and cycled  $\text{Bi}_{0.2}\text{Sr}_{0.8}\text{CoO}_{3-\delta}$ . Quantification of the EDX results is shown on the HAADF images. More EDX results for both pristine  $\text{Bi}_{0.2}\text{Sr}_{0.8}\text{CoO}_{3-\delta}$  and also fully charged and cycled  $\text{Bi}_{0.2}\text{Sr}_{0.8}\text{CoO}_{3-\delta}$  can be found in Figure S12.

(D) The bulk and surface Bi, Sr and Co metal composition in both pristine  $\text{Bi}_{0.2}\text{Sr}_{0.8}\text{CoO}_{3-\delta}$  and also charged and cycled  $\text{Bi}_{0.2}\text{Sr}_{0.8}\text{CoO}_{3-\delta}$  as determined by EDX. The error bars represent the standard deviation of at least eight spots.

Neither structural transformation (e.g. amorphization) nor compositional changes (e.g. metal leaching) were detected for  $\text{Bi}_{0.2}\text{Sr}_{0.8}\text{CoO}_{3-\delta}$  after galvanostatic charging and OER. We performed high-resolution transmission electron microscopy (HRTEM) imaging and energy-dispersive X-ray (EDX) elemental analysis (Figures 6 and S12) of  $\text{Bi}_{0.2}\text{Sr}_{0.8}\text{CoO}_{3-\delta}$  before and after galvanostatic charging (to  $\sim 1.4$  V vs. RHE at C/50, Figure S3) and OER measurements. No surface amorphization of charged  $\text{Bi}_{0.2}\text{Sr}_{0.8}\text{CoO}_{3-\delta}$  after OER was detected from HRTEM analysis (Figure 6B), Raman spectroscopy (Figure S13) and O K-edge XAS spectra (Figure S14), where the surface remained crystalline like the pristine  $\text{Bi}_{0.2}\text{Sr}_{0.8}\text{CoO}_{3-\delta}$  powder (Figure 6A). Such high surface stability of charged  $\text{Bi}_{0.2}\text{Sr}_{0.8}\text{CoO}_{3-\delta}$  after OER is in contrast to the rapid surface amorphization and the formation of surface hydroxides comprised of edge-sharing octahedra clusters found for  $\text{Ba}_{0.5}\text{Sr}_{0.5}\text{Co}_{0.8}\text{Fe}_{0.2}\text{O}_{3-\delta}$  and  $\text{SrCo}_{0.8}\text{Fe}_{0.2}\text{O}_{3-\delta}$  at OER potentials.<sup>66</sup> In addition,  $\text{Bi}_{0.2}\text{Sr}_{0.8}\text{CoO}_{3-\delta}$  after galvanostatic charging and OER appeared to be more stable than  $\text{SrCoO}_{3-\delta}$  as few nanometers of amorphous layers were detected on  $\text{SrCoO}_{3-\delta}$  particles after charging and OER measurements as reported recently.<sup>38</sup> Moreover, EDX elemental analysis (Figures 6C, 6D and S12) confirmed no A-site or B-site metal leaching after charging and OER, in contrast to the notable A-site metal leaching found in  $\text{Ba}_{0.5}\text{Sr}_{0.5}\text{Co}_{0.8}\text{Fe}_{0.2}\text{O}_{3-\delta}$ ,<sup>66</sup>  $\text{SrCo}_{0.8}\text{Fe}_{0.2}\text{O}_{3-\delta}$ ,<sup>66</sup> and  $\text{Sr}_x\text{Ca}_{1-x}\text{FeO}_{3-\delta}$  ( $x = 0, 0.5$  or  $1$ ).<sup>49</sup> Both bulk and surface metal ratios between A-site (Bi and Sr) and B-site (Co) metals of  $\text{Bi}_{0.2}\text{Sr}_{0.8}\text{CoO}_{3-\delta}$  before and after charging and OER measurements were found to be close to 1:4:5 as expected from the nominal stoichiometry. The high surface stability of charged  $\text{Bi}_{0.2}\text{Sr}_{0.8}\text{CoO}_{3-\delta}$  at OER potentials can be attributed to its lowered O 2p-band center with respect to the Fermi level (Figure 4C) in comparison to other highly active Co-based and Fe-based perovskites (such as  $\text{SrCoO}_{3-\delta}$  and  $\text{Ba}_{0.5}\text{Sr}_{0.5}\text{Co}_{0.8}\text{Fe}_{0.2}\text{O}_{3-\delta}$ ). The computed oxygen 2p-band centers of  $\text{Bi}_{0.125}\text{Sr}_{0.875}\text{CoO}_3$  and  $\text{Bi}_{0.25}\text{Sr}_{0.75}\text{CoO}_3$  were moved down by  $\sim 0.10$  eV and  $\sim 0.25$  eV relative to the Fermi level when compared with stoichiometric  $\text{SrCoO}_3$  (Figures 4B and 4C), respectively, which can



be attributed to the reduction of the nominal cobalt oxidation state (e.g. from +4 in  $\text{SrCoO}_3$  to +3.875 in  $\text{Bi}_{0.125}\text{Sr}_{0.875}\text{CoO}_3$  and +3.75 in  $\text{Bi}_{0.25}\text{Sr}_{0.75}\text{CoO}_3$ ) and thus the increase of cobalt 3d-band filling and the Fermi level (Figure 4A). Given that the O 2p-band center relative to the Fermi level can be correlated to the formation enthalpy of oxygen vacancies in perovskite oxides (Figure 4C),<sup>72</sup> lower O 2p-band centers of  $\text{Bi}_{0.125}\text{Sr}_{0.875}\text{CoO}_3$  and  $\text{Bi}_{0.25}\text{Sr}_{0.75}\text{CoO}_3$  relative to the Fermi level would have higher energy penalty for the creation of oxygen vacancies in the perovskite structure than that of  $\text{SrCoO}_3$ , indicative of greater structural stability (Figure S15).

In this study, we report the record intrinsic OER activity and high surface stability of the fully charged  $\text{Bi}_{0.2}\text{Sr}_{0.8}\text{CoO}_{3-\delta}$  ( $\delta \approx 0$ ) perovskite oxide in alkaline electrolyte. We show that the inductive effect associated with rational bismuth substitution results in marked increase of the intrinsic OER catalytic activity, exceeding those of other Co-based perovskite oxides reported to date, including charged  $\text{SrCoO}_{3-\delta}$ , at high current densities ( $> \sim 1 \text{ mA cm}^{-2}_{\text{oxide}}$ ). Although  $\text{Bi}^{3+}$  substitution (i.e. replacing  $\text{Sr}^{2+}$  with  $\text{Bi}^{3+}$ ) reduced the cobalt oxidation state and thus lowered the oxygen 2p band relative to the Fermi level, DFT computations show that high Co-O covalency maintained due to the inductive effect from  $\text{Bi}^{3+}$  and is comparable with charged  $\text{SrCoO}_{3-\delta}$ . As the OER kinetics of highly covalent oxides are limited by the chemical or electrochemical deprotonation at the oxide surface due to weak hydroxide affinity, the high OER activity of charged  $\text{Bi}_{0.2}\text{Sr}_{0.8}\text{CoO}_{3-\delta}$  can be attributed to the enhanced affinity towards hydroxide ions due to the presence of strongly Lewis acidic A-site  $\text{Bi}^{3+}$  ions on the perovskite surface. In addition, the observed pH dependence of the pre-OER redox peaks and OER activity on the RHE scale implies non-concerted proton-electron transfer pathways and pH-dependent binding of intermediates, however further in-situ diffraction and spectroscopic studies are needed to provide further detailed insights into the surface species and rate-limiting step. Moreover, neither structural or chemical changes have been found for  $\text{Bi}_{0.2}\text{Sr}_{0.8}\text{CoO}_{3-\delta}$  after galvanostatic charging and

OER, and the high surface stability can be attributed to higher energy penalty for the creation of oxygen vacancies due to the lower oxygen 2p band relative to the Fermi level. Demonstrating how leveraging the inductive effect associated with metal substitution enhances the specific activity of highly OER-active cobalt-based perovskites through maintaining high metal-oxygen covalency and strengthening hydroxide affinity without the expense of surface stability, this work highlights new prospects for the rational design of novel catalysts for electrochemical energy conversion and storage.

## **EXPERIMENTAL PROCEDURES**

For full details please refer to Supplemental Experimental Procedure.

## **SUPPLEMENTAL INFORMATION**

Supplemental Information includes Supplemental Experimental Procedures, 16 figures, and 2 tables and can be found with this article online.

## **ACKNOWLEDGMENTS**

This work was supported by the Toyota Research Institute through the Accelerated Materials Design and Discovery program. The authors are grateful to Dr. Juan Corchado Garcia and Jonathan Hwang for performing O K-edge XAS measurements and data analysis. The authors are grateful to Yang Yu and Pinar Karayaylali for performing Co K-edge XAS measurements and data analysis. This research used resources of the National Energy Research Scientific Computing Center, a DOE Office of Science User Facility supported by the Office of Science of the U.S. Department of Energy under Contract No. DE-AC02-05CH11231. This work also used resources of the Extreme Science and Engineering Discovery Environment (XSEDE),<sup>73</sup> which is supported by National Science Foundation grant number ACI-1548562. This work made use of the MRSEC Shared

Experimental Facilities at MIT, supported by the National Science Foundation under award number DMR-1419807.

## **AUTHOR CONTRIBUTIONS**

Y.S.-H. and D.A.K. conceived the project. D.A.K., Y.S.-H. and J.P. designed the experiments. D.A.K. carried out the synthesis and structural characterization. D.A.K. and J.P. performed the electrochemical measurements. J.P. performed the TEM analysis. J.P. and L.G. carried out the DFT calculations. D.A.K. and J.P. prepared the initial draft. All authors contributed to the discussions and revisions of the manuscript.

## **DECLARATION OF INTERESTS**

The authors declare no competing interests.

## **REFERENCES**

1. Seh, Z.W., Kibsgaard, J., Dickens, C.F., Chorkendorff, I., Nørskov, J.K., and Jaramillo, T.F. (2017). Combining theory and experiment in electrocatalysis: Insights into materials design. *Science* 355, eaad4998.
2. McCrory, C.C.L., Jung, S., Ferrer, I.M., Chatman, S.M., Peters, J.C., and Jaramillo, T.F. (2015). Benchmarking Hydrogen Evolving Reaction and Oxygen Evolving Reaction Electrocatalysts for Solar Water Splitting Devices. *J. Am. Chem. Soc.* 137, 4347–4357.
3. Montoya, J.H., Seitz, L.C., Chakthranont, P., Vojvodic, A., Jaramillo, T.F., and Nørskov, J.K. (2017). Materials for solar fuels and chemicals. *Nat. Mater.* 16, 70–81.
4. Morales-Guio, C.G., Cave, E.R., Nitopi, S.A., Feaster, J.T., Wang, L., Kuhl, K.P., Jackson, A., Johnson, N.C., Abram, D.N., Hatsukade, T., *et al.* (2018). Improved CO<sub>2</sub> reduction activity towards C<sub>2</sub>+ alcohols on a tandem gold on copper electrocatalyst. *Nat. Catal.* 1, 764–771.

5. Dunn, B., Kamath, H., and Tarascon, J.-M. (2011). Electrical Energy Storage for the Grid: A Battery of Choices. *Science* 334, 928.
6. Goodenough, J.B., and Park, K.-S. (2013). The Li-Ion Rechargeable Battery: A Perspective. *J. Am. Chem. Soc.* 135, 1167–1176.
7. Turcheniuk, K., Bondarev, D., Singhal, V., and Yushin, G. (2018). Ten years left to redesign lithium-ion batteries. *Nature* 559, 467–470.
8. Rossmeisl, J., Qu, Z.W., Zhu, H., Kroes, G.J., and Nørskov, J.K. (2007). Electrolysis of water on oxide surfaces. *J. Electroanal. Chem.* 607, 83–89.
9. Man, I.C., Su, H.Y., Calle-Vallejo, F., Hansen, H.A., Martínez, J.I., Inoglu, N.G., Kitchin, J., Jaramillo, T.F., Nørskov, J.K., and Rossmeisl, J. (2011). Universality in oxygen evolution electrocatalysis on oxide surfaces. *ChemCatChem* 3, 1159–1165.
10. Dau, H., Limberg, C., Reier, T., Risch, M., Roggan, S., and Strasser, P. (2010). The mechanism of water oxidation: from electrolysis via homogeneous to biological catalysis. *ChemCatChem* 2, 724–761.
11. Lee, Y., Suntivich, J., May, K.J., Perry, E.E., and Shao-Horn, Y. (2012). Synthesis and activities of rutile IrO<sub>2</sub> and RuO<sub>2</sub> nanoparticles for oxygen evolution in acid and alkaline solutions. *J. Phys. Chem. Lett.* 3, 399–404.
12. Fang, Y., and Liu, Z. (2010). Mechanism and Tafel lines of electro-oxidation of water to oxygen on RuO<sub>2</sub>(110). *J. Am. Chem. Soc.* 132, 18214–18222.
13. Sanchez Casalongue, H.G., Ng, M.L., Kaya, S., Friebe, D., Ogasawara, H., and Nilsson, A. (2014). In situ observation of surface species on iridium oxide nanoparticles during the oxygen evolution reaction. *Angew. Chem. Int. Ed.* 53, 7169–7172.
14. Bernicke, M., Ortel, E., Reier, T., Bergmann, A., Ferreira De Araujo, J., Strasser, P., and Kraehnert, R. (2015). Iridium oxide coatings with templated porosity as highly active oxygen evolution catalysts: structure-activity relationships. *ChemSusChem* 8, 1908–1915.
15. Du, P., and Eisenberg, R. (2012). Catalysts made of earth-abundant elements (Co, Ni, Fe) for water splitting: recent progress and future challenges. *Energy Environ. Sci.* 5, 6012–6021.

16. Suen, N.-T., Hung, S.-F., Quan, Q., Zhang, N., Xu, Y.-J., and Chen, H.M. (2017). Electrocatalysis for the oxygen evolution reaction: recent development and future perspectives. *Chem. Soc. Rev.* *46*, 337–365.
17. Bockris, J.O., and Otagawa, T. (1984). The Electrocatalysis of Oxygen Evolution on Perovskites. *J. Electrochem. Soc.* *131*, 290–302.
18. Matsumoto, Y., and Sato, E. (1986). Electrocatalytic properties of transition metal oxides for oxygen evolution reaction. *Mater. Chem. Phys.* *14*, 397–426.
19. Wei, C., Feng, Z., Scherer, G.G., Barber, J., Shao-Horn, Y., and Xu, Z.J. (2017). Cations in Octahedral Sites: A Descriptor for Oxygen Electrocatalysis on Transition-Metal Spinel. *Adv. Mater.* *29*, 1606800.
20. Kanan, M.W., Surendranath, Y., and Nocera, D.G. (2009). Cobalt–phosphate oxygen-evolving compound. *Chem. Soc. Rev.* *38*, 109–114.
21. Burke, M.S., Enman, L.J., Batchellor, A.S., Zou, S., and Boettcher, S.W. (2015). Oxygen Evolution Reaction Electrocatalysis on Transition Metal Oxides and (Oxy)hydroxides: Activity Trends and Design Principles. *Chem. Mater.* *27*, 7549–7558.
22. Trześniewski, B.J., Diaz-Morales, O., Vermaas, D.A., Longo, A., Bras, W., Koper, M.T.M., and Smith, W.A. (2015). In Situ Observation of Active Oxygen Species in Fe-Containing Ni-Based Oxygen Evolution Catalysts: The Effect of pH on Electrochemical Activity. *J. Am. Chem. Soc.* *137*, 15112–15121.
23. Burke, M.S., Kast, M.G., Trotochaud, L., Smith, A.M., and Boettcher, S.W. (2015). Cobalt-iron (oxy)hydroxide oxygen evolution electrocatalysts: the role of structure and composition on activity, stability, and mechanism. *J. Am. Chem. Soc.* *137*, 3638–3648.
24. Kanan, M.W., and Nocera, D.G. (2008). In Situ Formation of an Oxygen-Evolving Catalyst in Neutral Water Containing Phosphate and  $\text{Co}^{2+}$ . *Science* *321*, 1072–1075.
25. Dincă, M., Surendranath, Y., and Nocera, D.G. (2010). Nickel-borate oxygen-evolving catalyst that functions under benign conditions. *Proc. Natl. Acad. Sci.* *107*, 10337.

26. Trotochaud, L., Ranney, J.K., Williams, K.N., and Boettcher, S.W. (2012). Solution-Cast Metal Oxide Thin Film Electrocatalysts for Oxygen Evolution. *J. Am. Chem. Soc.* *134*, 17253–17261.
27. Ng, J.W.D., Garcia-Melchor, M., Bajdich, M., Chakthranont, P., Kirk, C., Vojvodic, A., and Jaramillo, T.F. (2016). Gold-supported cerium-doped NiOx catalysts for water oxidation. *Nat. Energy* *1*, 16053.
28. Kuznetsov, D.A., Han, B., Yu, Y., Rao, R.R., Hwang, J., Román-Leshkov, Y., and Shao-Horn, Y. (2018). Tuning Redox Transitions via Inductive Effect in Metal Oxides and Complexes, and Implications in Oxygen Electrocatalysis. *Joule* *2*, 225–244.
29. Friebe, D., Louie, M.W., Bajdich, M., Sanwald, K.E., Cai, Y., Wise, A.M., Cheng, M.-J., Sokaras, D., Weng, T.-C., Alonso-Mori, R., *et al.* (2015). Identification of Highly Active Fe Sites in (Ni,Fe)OOH for Electrocatalytic Water Splitting. *J. Am. Chem. Soc.* *137*, 1305–1313.
30. Chemelewski, W.D., Lee, H.-C., Lin, J.-F., Bard, A.J., and Mullins, C.B. (2014). Amorphous FeOOH Oxygen Evolution Reaction Catalyst for Photoelectrochemical Water Splitting. *J. Am. Chem. Soc.* *136*, 2843–2850.
31. Hong, W.T., Risch, M., Stoerzinger, K.A., Grimaud, A., Suntivich, J., and Shao-Horn, Y. (2015). Toward the rational design of non-precious transition metal oxides for oxygen electrocatalysis. *Energy Environ. Sci.* *8*, 1404–1427.
32. Grimaud, A., May, K.J., Carlton, C.E., Lee, Y.-L., Risch, M., Hong, W.T., Zhou, J., and Shao-Horn, Y. (2013). Double perovskites as a family of highly active catalysts for oxygen evolution in alkaline solution. *Nat. Commun.* *4*, 2439.
33. Suntivich, J., May, K.J., Gasteiger, H.A., Goodenough, J.B., and Shao-Horn, Y. (2011). A Perovskite Oxide Optimized for Oxygen Evolution Catalysis from Molecular Orbital Principles. *Science* *334*, 1383–1385.
34. Hwang, J., Rao, R.R., Giordano, L., Katayama, Y., Yu, Y., and Shao-Horn, Y. (2017). Perovskites in catalysis and electrocatalysis. *Science* *358*, 751.
35. Grimaud, A., Demortière, A., Saubanère, M., Dachraoui, W., Duchamp, M., Doublet, M.-L., and Tarascon, J.-M. (2016). Activation of surface oxygen sites on an iridium-based model catalyst for the oxygen evolution reaction. *Nat. Energy* *2*, 16189.

36. Kim, Y.-T., Lopes, P.P., Park, S.-A., Lee, A.-Y., Lim, J., Lee, H., Back, S., Jung, Y., Danilovic, N., Stamenkovic, V., *et al.* (2017). Balancing activity, stability and conductivity of nanoporous core-shell iridium/iridium oxide oxygen evolution catalysts. *Nat. Commun.* **8**, 1449.
37. Hong, W., Stoerzinger, K.A., Lee, Y.-L., Giordano, L., Grimaud, A.J.L., Johnson, A.M., Hwang, J., Crumlin, E., Yang, W., and Shao-Horn, Y. (2017). Charge-transfer-energy-dependent oxygen evolution reaction mechanisms for perovskite oxides. *Energy Environ. Sci.* **10**, 2190–2200.
38. Grimaud, A., Diaz-Morales, O., Han, B., Hong, W.T., Lee, Y.L., Giordano, L., Stoerzinger, K.A., Koper, M.T.M., and Shao-Horn, Y. (2017). Activating lattice oxygen redox reactions in metal oxides to catalyze oxygen evolution. *Nat. Chem.* **9**, 457–465.
39. Portier, J., Poizot, P., Campet, G., Subramanian, M.A., and Tarascon, J.-M. (2003). Acid–base behavior of oxides and their electronic structure. *Solid State Sci.* **5**, 695–699.
40. Matar, S.F., Campet, G., and Subramanian, M.A. (2011). Electronic properties of oxides: Chemical and theoretical approaches. *Prog. Solid State Chem.* **39**, 70–95.
41. Yang, C., Laberty-Robert, C., Batuk, D., Cibir, G., Chadwick, A.V., Pimenta, V., Yin, W., Zhang, L., Tarascon, J.-M., and Grimaud, A. (2017). Phosphate Ion Functionalization of Perovskite Surfaces for Enhanced Oxygen Evolution Reaction. *J. Phys. Chem. Lett.* **8**, 3466–3472.
42. Hong, W.T., Welsch, R.E., and Shao-Horn, Y. (2016). Descriptors of oxygen-evolution activity for oxides: a statistical evaluation. *J. Phys. Chem. C* **120**, 78–86.
43. Dean, J.A. (1999). *Lange’s Handbook of Chemistry*.
44. Mefford, J.T., Rong, X., Abakumov, A.M., Hardin, W.G., Dai, S., Kolpak, A.M., Johnston, K.P., and Stevenson, K.J. (2016). Water electrolysis on  $\text{La}_{1-x}\text{Sr}_x\text{CoO}_{3-\delta}$  perovskite electrocatalysts. *Nat. Commun.* **7**, 11053.
45. Knee, C.S., Lindberg, F., Khan, N., Svensson, G., Svedlindh, P., Rundlöf, H., Eriksson, S.G., and Börjesson, L. (2006). Influence of oxygen defects on the structure and magnetic properties of  $\text{Sr}_{1-x}\text{Bi}_x\text{CoO}_{3-y}$  ( $0.1 \leq x \leq 0.2$ ) supercell perovskites. *Chem. Mater.* **18**, 1354–1364.

46. Stoerzinger, K.A., Renshaw Wang, X., Hwang, J., Rao, R.R., Hong, W.T., Rouleau, C.M., Lee, D., Yu, Y., Crumlin, E.J., and Shao-Horn, Y. (2018). Speciation and Electronic Structure of  $\text{La}_{1-x}\text{Sr}_x\text{CoO}_{3-\delta}$  During Oxygen Electrolysis. *Top. Catal.* **61**, 2161–2174.
47. Nemudry, A., Rudolf, P., and Schöllhorn, R. (1996). Topotactic electrochemical redox reactions of the defect perovskite  $\text{SrCoO}_{2.5+x}$ . *Chem. Mater.* **8**, 2232–2238.
48. Grenier, J.-C., Wattiaux, A., Doumerc, J.-P., Dordor, P., Fournes, L., Chaminade, J.-P., and Pouchard, M. (1992). Electrochemical oxygen intercalation into oxide networks. *J. Solid State Chem.* **96**, 20–30.
49. Han, B., Grimaud, A., Giordano, L., Hong, W.T., Diaz-Morales, O., Yueh-Lin, L., Hwang, J., Charles, N., Stoerzinger, K.A., Yang, W., *et al.* (2018). Iron-based perovskites for catalyzing oxygen evolution reaction. *J. Phys. Chem. C* **122**, 8445–8454.
50. Mizushima, K., Jones, P.C., Wiseman, P.J., and Goodenough, J.B. (1980).  $\text{Li}_x\text{CoO}_2$  ( $0 < x \leq 1$ ): A new cathode material for batteries of high energy density. *Mater. Res. Bull.* **15**, 783–789.
51. Han, B., Qian, D., Risch, M., Chen, H., Chi, M., Meng, Y.S., and Shao-Horn, Y. (2015). Role of  $\text{LiCoO}_2$  surface terminations in oxygen reduction and evolution kinetics. *J. Phys. Chem. Lett.* **6**, 1357–1362.
52. Tarascon, J.M., Ramesh, R., Barboux, P., Hedge, M.S., Hull, G.W., Greene, L.H., Giroud, M., LePage, Y., McKinnon, W.R., Waszczak, J. V., *et al.* (1989). New non-superconducting layered Bi-oxide phases of formula  $\text{Bi}_2\text{M}_3\text{Co}_2\text{O}_y$  containing Co instead of Cu. *Solid State Commun.* **71**, 663–668.
53. Rossmeisl, J., Logadottir, A., and Nørskov, J.K. (2005). Electrolysis of water on (oxidized) metal surfaces. *Chem. Phys.* **319**, 178–184.
54. Goodenough, J.B., Manoharan, R., and Paranthaman, M. (1990). Surface protonation and electrochemical activity of oxides in aqueous solution. *J. Am. Chem. Soc.* **112**, 2076–2082.
55. Koper, M.T.M. (2013). Theory of the transition from sequential to concerted electrochemical proton–electron transfer. *Phys. Chem. Chem. Phys.* **15**, 1399–1407.



56. Giordano, L., Han, B., Risch, M., Hong, W.T., Rao, R.R., Stoerzinger, K.A., and Shao-Horn, Y. (2016). pH dependence of OER activity of oxides: current and future perspectives. *Catal. Today* 262, 2–10.
57. Gorlin, M., De Araujo, J.F., Schmies, H., Bernsmeier, D., Dresp, S., Gliech, M., Jusys, Z., Chernev, P., Kraehnert, R., Dau, H., *et al.* (2017). Tracking catalyst redox states and reaction dynamics in Ni-Fe oxyhydroxide oxygen evolution reaction electrocatalysts: the role of catalyst support and electrolyte pH. *J. Am. Chem. Soc.* 139, 2070–2082.
58. Schwarz, K., Xu, B., Yan, Y., and Sundararaman, R. (2016). Partial oxidation of step-bound water leads to anomalous pH effects on metal electrode step-edges. *Phys. Chem. Chem. Phys.* 18, 16216–16223.
59. van der Niet, M.J.T.C., Garcia-Araez, N., Hernández, J., Feliu, J.M., and Koper, M.T.M. (2013). Water dissociation on well-defined platinum surfaces: the electrochemical perspective. *Catal. Today* 202, 105–113.
60. Gisbert, R., García, G., and Koper, M.T.M. (2010). Adsorption of phosphate species on poly-oriented Pt and Pt(111) electrodes over a wide range of pH. *Electrochimica Acta* 55, 7961–7968.
61. Zhang, M., De Respinis, M., and Frei, H. (2014). Time-resolved observations of water oxidation intermediates on a cobalt oxide nanoparticle catalyst. *Nat. Chem.* 6, 362–367.
62. Gerken, J.B., McAlpin, J.G., Chen, J.Y.C., Rigsby, M.L., Casey, W.H., Britt, R.D., and Stahl, S.S. (2011). Electrochemical water oxidation with cobalt-based electrocatalysts from pH 0–14: the thermodynamic basis for catalyst structure, stability, and activity. *J. Am. Chem. Soc.* 133, 14431–14442.
63. Stoerzinger, K.A., Rao, R.R., Wang, X.R., Hong, W.T., Rouleau, C.M., and Shao-Horn, Y. (2017). The role of Ru redox in pH-dependent oxygen evolution on rutile ruthenium dioxide surfaces. *Chem* 2, 668–675.
64. Kuo, D.-Y., Kawasaki, J.K., Nelson, J.N., Kloppenburg, J., Hautier, G., Shen, K.M., Schlom, D.G., and Suntivich, J. (2017). Influence of surface adsorption on the oxygen evolution reaction on IrO<sub>2</sub>(110). *J. Am. Chem. Soc.* 139, 3473–3479.
65. Watanabe, E., Rossmeisl, J., Björketun, M.E., Ushiyama, H., and Yamashita, K. (2016). Atomic-scale analysis of the RuO<sub>2</sub>/water interface under electrochemical conditions. *J. Phys. Chem. C* 120, 8096–8103.

66. May, K.J., Carlton, C.E., Stoerzinger, K.A., Risch, M., Suntivich, J., Lee, Y.L., Grimaud, A., and Shao-Horn, Y. (2012). Influence of oxygen evolution during water oxidation on the surface of perovskite oxide catalysts. *J. Phys. Chem. Lett.* **3**, 3264–3270.
67. Gong, M., Li, Y., Wang, H., Liang, Y., Wu, J.Z., Zhou, J., Wang, J., Regier, T., Wei, F., and Dai, H. (2013). An Advanced Ni–Fe Layered Double Hydroxide Electrocatalyst for Water Oxidation. *J. Am. Chem. Soc.* **135**, 8452–8455.
68. Shinagawa, T., Garcia-Esparza, A.T., and Takanabe, K. (2015). Insight on Tafel slopes from a microkinetic analysis of aqueous electrocatalysis for energy conversion. *Sci. Rep.* **5**, 13801.
69. Rao, R.R., Kolb, M.J., Halck, N.B., Pedersen, A.F., Mehta, A., You, H., Stoerzinger, K.A., Feng, Z., Hansen, H.A., Zhou, H., *et al.* (2017). Towards identifying the active sites on RuO<sub>2</sub>(110) in catalyzing oxygen evolution. *Energy Environ. Sci.* **10**, 2626–2637.
70. Katayama, Y., Nattino, F., Giordano, L., Hwang, J., Rao, R.R., Andreussi, O., Marzari, N., and Shao-Horn, Y. (2018). An In Situ Surface-Enhanced Infrared Absorption Spectroscopy Study of Electrochemical CO<sub>2</sub> Reduction: Selectivity Dependence on Surface C-Bound and O-Bound Reaction Intermediates. *J. Phys. Chem. C*. Available at: <https://doi.org/10.1021/acs.jpcc.8b09598>.
71. Katayama, Y., Giordano, L., Rao, R.R., Hwang, J., Muroyama, H., Matsui, T., Eguchi, K., and Shao-Horn, Y. (2018). Surface (Electro)chemistry of CO<sub>2</sub> on Pt Surface: An in Situ Surface-Enhanced Infrared Absorption Spectroscopy Study. *J. Phys. Chem. C* **122**, 12341–12349.
72. Lee, Y.L., Kleis, J., Rossmeisl, J., Shao-Horn, Y., and Morgan, D. (2011). Prediction of solid oxide fuel cell cathode activity with first-principles descriptors. *Energy Environ. Sci.* **4**, 3966–3970.
73. Towns, J., Cockerill, T., Dahan, M., Foster, I., Gaither, K., Grimshaw, A., Hazlewood, V., Lathrop, S., Lifka, D., Peterson, G., *et al.* (2014). XSEDE: accelerating scientific discovery. *Comput. Sci. Eng.* **16**, 62–74.